



Dense and strong, but superinsulating silica aerogel

Subramaniam Iswar^{a,b}, Sandra Galmarini^a, Luca Bonanomi^{c,d}, Jannis Wernery^a, Eleftheria Roumeli^{c,d}, Sudheera Nimalshantha^a, Avner M. Ben Ishai^a, Marco Lattuada^b, Matthias M. Koebel^a, Wim J. Malfait^{a,*}

^a Laboratory for Building Energy Materials and Components, Swiss Federal Laboratories for Science and Technology, Empa, Überlandstrasse 129, 8600 Dübendorf, Switzerland

^b University of Fribourg, Department of Chemistry, Chemin du Musée 9, 1700 Fribourg, Switzerland

^c Department of Mechanical and Process Engineering, ETH Zürich, Tannenstrasse 3, 8092 Zürich, Switzerland

^d Division of Engineering and Applied Science, California Institute of Technology, Pasadena, CA 91125, USA

ARTICLE INFO

Article history:

Received 19 January 2021

Revised 21 April 2021

Accepted 30 April 2021

Available online 9 May 2021

Keywords:

Silica aerogel

Evaporative drying

Shrinkage

Thermal conductivity

Uniaxial compression

ABSTRACT

Silica aerogel is the ultimate thermal insulator thanks to its record-breaking low thermal conductivity (λ), open porosity and hydrophobicity. Silica aerogel's thermal conductivity is lowest at intermediate densities ($\rho \approx 0.11 \text{ g/cm}^3$) and, because of the strong, power-law dependence of the E modulus on density, this rather low density so far led to low E moduli. Even with polymer reinforcement, increasing stiffness is only possible at higher density, thus higher conductivity. This paper explores the synthesis of silica aerogel granules using ambient pressure drying to provide enhanced mechanical stiffness whilst maintaining thermal conductivities well below $20 \text{ mW m}^{-1} \text{ K}^{-1}$. The aging and drying conditions affect the interplay between mechanical and thermal properties, and are varied to optimize the physical properties. The dense ($\rho \leq 0.29 \text{ g/cm}^3$), but superinsulating ($\lambda \approx 15 \text{ mW m}^{-1} \text{ K}^{-1}$) silica aerogels presented in this paper challenge the community's understanding of heat transport in aerogels, and do not rely on polymer reinforcement. The underlying microscopic structural parameters affecting the mechanical and thermal transport properties are investigated by modelling and simulation of the aerogel back-bone. Short aging times reduce the cross-section of, and heat transport through, inter-particle necks, leading to an overall decrease in thermal conductivity through the solid skeleton (λ_s). In addition, short-aged gels undergo a partial pore collapse during ambient pressure drying of the pore fluid due to less aged, hence weaker network structures. The resulting denser structure contains additional point contacts that increase stiffness, by up to an order of magnitude. However, heat transport through these newly formed point-contacts is limited and the gas phase conduction (λ_g) is further suppressed due to the even smaller pore sizes. Strong and superinsulating particles are ideal fillers for aerogel composites, concrete and renders. The optimized APD aerogels, available as granules, are finally compiled in a composite thermal insulation board with an effective thermal conductivity down to $20 \text{ mW m}^{-1} \text{ K}^{-1}$ with improved strength: a 2-fold increase for E , compared to a board produced from classical silica aerogel granulate. The possibility to improve mechanical properties of pure silica aerogels can help aerogels to break into new high-strength, superinsulating structural applications needed to reduce carbon emissions of the built environment.

© 2021 The Author(s). Published by Elsevier Ltd on behalf of Acta Materialia Inc.

This is an open access article under the CC BY license (<http://creativecommons.org/licenses/by/4.0/>)

1. Introduction

Aerogels [1,2] have unique material properties (λ , ρ , surface area) and a range of applications [3–9], most notably as thermal insulation [10]. Although silica aerogels constitute a global market of ~300 Mio US\$ per annum, their potential is restricted by their

low stiffness and high brittleness [11]. Silica aerogel blankets, comprising of silica aerogel embedded in a glass or polymer fiber felts, enable a wider range of application and are the most commonly sold aerogel product today. Also the silica aerogel phase itself can be reinforced: a wide body of scientific and patent literature exists on reinforcement with organosilanes, synthetic or biopolymers [12–19], but a strong increase of E most often still requires a simultaneous increase in density, which in turn increases thermal conductivity [20–24].

* Corresponding author.

E-mail address: wim.malfait@empa.ch (W.J. Malfait).

The mechanical properties of silica aerogels strongly depend on their density with three domains in terms of their response to uniaxial compression [24]. At low densities, silica aerogels are non-brittle, very compressible, and deform plastically: under controlled laboratory conditions, low-density silica aerogels can be compressed to relative strain values well in excess of 50%, without brittle rupture, but the deformation is almost entirely permanent and the materials do not recover their original volume after the load has been removed. At intermediate densities, silica aerogels are brittle, but the deformation becomes increasingly elastic with increasing density and the aerogels can recover most of the strain upon decompression. High density silica aerogels are very brittle, but much less compressible than low to intermediate density aerogels. As is typical for most aerogel systems [22,25], the E-modulus of classical silica aerogel displays a strong power-law dependence on density $E \sim \rho^\alpha$, with values for α in the range of 2.6–3.7 [24,26–29]. Aside from density as the first-order control on the mechanical control, other parameters also affect the mechanical properties, including the synthesis conditions (e.g. aging) and microstructure. The experimentally derived mechanical properties of aerogels have long been interpreted analytically, but recent numerical simulations of aerogel structures and properties are starting to provide insight into the deformation mechanisms [27–34].

Thermal transport through aerogels occurs through the gas phase, the solid particle network, and radiation^{15,16}. Aerogels owe their extremely low thermal conductivity to a unique combination of intermediate density, small pores and high solid network tortuosity [35]. At low density, the pores are large and λ_g remains high, but with increasing density, the pores become smaller than the mean free path length of the gas (~70 nm for air at room temperature) and λ_g is strongly reduced through the Knudsen effect. Conversely, λ_s through the silica skeletal particle network increases with increasing density [35]. Radiative contributions to thermal conductivity are generally lower and decrease with increasing density. To produce the lowest λ materials, it is thus necessary to find the best compromise among these contributions, leading to the current paradigm that aerogel materials display a minimum in thermal conductivity at intermediate density: at ~0.11 g/cm³ for silica aerogels [21,23,24], at ~0.16 g/cm³ for resorcinol-formaldehyde aerogels [20,23,36], and at ~0.20–0.22 g/cm³ for polyurea and polyurethane aerogels [37,38]. Some exceptional, organic-inorganic hybrid aerogels have been reported with low thermal conductivities at relatively high density (~15 mW m⁻¹ K⁻¹ at 0.160–0.220 g/cm³) [39,40], but no pure silica aerogels have been reported with $\lambda < 17$ mW m⁻¹ K⁻¹ for $\rho > 0.20$ g/cm³.

In this work, we first investigate silica aerogel cylinders prepared by supercritical drying (SCD) to evaluate the effects of density and aging on the mechanical properties and thermal conductivity (Scheme 1). We then describe a modified fabrication route, based on ambient pressure drying (APD), that enables the production of silica aerogel granulate with a very low thermal conductivity (~15 mW m⁻¹ K⁻¹) at twice the density (0.24 versus 0.12 g/cm³) and up to an order of magnitude higher stiffness of standard silica aerogel. The comparison of the SCD and APD results, combined with numerical simulations of thermal conductivity, highlight the importance of inter-particle necks for heat conduction. Finally, glued composites prepared from the stiff, thermally superinsulating silica aerogel granulate retain the exceptional mechanical and thermal properties.

2. Materials and methods

2.1. Silica aerogel synthesis

All silica aerogels were prepared according to the process scheme as described by Iswar et al. [41] and the materials de-

scribed here are very similar. Here, we focus on the thermal conductivity and mechanical properties of SCD and APD aerogels (Scheme 1). The gelation of an ethanolic sol containing colloidal, pre-polymerized tetraethyl orthosilicate (TEOS) [42] was initiated by the addition of a base catalyst, followed by aging, hydrophobization (silylation) with acidified hexamethyldisiloxane, and ambient pressure (APD) [43] or supercritical CO₂ drying (SCD). The gels intended for SCD were aged at 65°C for either 2 or 24 hours, and aerogels of varying ρ were obtained by varying the starting SiO₂ equivalent concentration (0.038–0.171 g/cm³). The gels intended for APD were aged for 2, 4, 6, 8, 16 or 24 h for a fixed SiO₂ equivalent concentration in the sol of 0.057 g/cm³. For e.g., for a silica precursor concentration of 0.057 g/cm³, 9 ml of polyethoxydisiloxane (PEDS), a pre-polymerized form of tetraethyl orthosilicate (TEOS) (referred to as PEDS-P_{750E20}) was diluted with 21 ml of ethanol and with 1 ml of distilled water under constant stirring conditions for 5–10 min at room temperature. Gelation occurred approximately 10 min after the addition of 0.36 ml of 5.5 M ammonium hydroxide solution (NH₄OH in water). The gels were covered with an additional 0.4 ml of ethanol to prevent exposure to the air due to solvent evaporation during aging, and aged at different times at 65°C. The aged gels were hydrophobized by soaking them in a mixture of 60 ml of hexamethyldisiloxane (HMDSO), 0.24 ml of concentrated hydrochloric acid (37% purity) and 2.2 ml of ethanol at 65°C for 24 h. The hydrophobized gels were dried at ambient pressure for 2h at 150°C. Additionally, the hydrophobized silica gels of varying densities were dried in an autoclave (4334/A21-1, Separex, France) from supercritical carbon dioxide (SCD).

From the same series of differently aged gels, APD aerogel granulate with a range of envelope ρ were obtained due to the aging time dependent partial pore collapse during drying [41]. The aerogels were characterized in terms of ρ , λ , surface area (S_{BET}), E and stiffness. Aerogels prepared under near-identical conditions were studied previously by SEM, TEM, SAXS and solid-state NMR and are fully amorphous [41].

2.2. Density and pore size analysis

The bulk density (ρ) of monolithic SCD aerogel samples was calculated from the weight and envelope volume. The bulk density of APD silica aerogel granulate was obtained by a Geopyc 1360 (Micromeritics). A 12.7 mm diameter chamber was used to measure with a consolidation force of 4 N. 10 cycles were carried out for each measurement. The specific surface area (S_{BET}) was determined from the nitrogen sorption isotherms (Micromeritics TriFlex) using Brunauer–Emmet–Teller (BET) analysis [44]. The specific pore volume (V_{pore}) was calculated from the bulk and skeletal density of the aerogel ($V_{\text{pore}} = (1/\rho_{\text{bulk}}) - (1/\rho_{\text{skeletal}})$) and a skeletal density of approximately 2.0 g/cm³ was used [45]. The average pore diameter was calculated from the pore volume and surface area ($D_{\text{pore}} = (4 \cdot V_{\text{pore}})/S_{\text{BET}}$) rather than the Barrett–Joyner–Halenda (BJH) analysis [46], which for aerogels is affected by mechanical deformation in the desorption branch of the capillary condensation range and is in effect a second drying of the gel from liquid nitrogen including a deformation with spring-back [47].

2.3. Thermal conductivity

The thermal conductivity (λ) of SCD monolithic square plate silica aerogels (EN 12667 at 10°C) was determined directly with a custom built guarded hot plate device specifically designed for small samples of low λ materials. This device has been described in detail in a previous study [48]. The thermal conductivity measurement is more complex for the APD materials, because they are only available in particulate form. The thermal conductivity of a

packed bed APD silica aerogel, in a 63:37 granulate:powder ratio, optimized to minimize the effect of air-pockets between the grains [49] was measured using the same guarded hot plate device. The intrinsic thermal conductivity of APD silica aerogel granulate was determined from the values derived of the packed bed using previously described calibration procedures [49]. Briefly, reference SCD silica aerogel monoliths of variable density, hence variable thermal conductivity, were produced. The thermal conductivity of the plates was determined by guarded hot-plate. The monoliths were subsequently broken up in to granulate and powder and the thermal conductivity of the packed bed was determined using the same mixing ratio, packing procedure and measurement conditions to cancel out the often large effects of the bed properties [50] as much as possible. Note that for our measurements, the effect of interstitial air has already been reduced by using an optimized mixing ratio between granules and powder. As a result, the packed-bed measurements were higher than that of the monolithic plates by only 1.4 to 2.3 $\text{mW m}^{-1} \text{K}^{-1}$. For packed beds of granules with a narrow particle size distribution, the volume of interstitial air is much higher and the packed bed thermal conductivities can be up to 10 $\text{mW m}^{-1} \text{K}^{-1}$ higher than those of a compacted bed or the aerogel material itself [50, 51]. The combined data on the reference aerogels, measured both in monolithic and packed-bed form, is the basis for a calibration curve that enables the calculation of the intrinsic thermal conductivity from the packed-bed measurements [49]. Note that the magnitude of the correction needed to go from packed-bed to intrinsic thermal conductivity is on the order of $2 \pm 1 \text{ mW m}^{-1} \text{K}^{-1}$, i.e. less than half of the observed effect size of the partial pore collapse (see below). Although the uncertainty on the accuracy of the guarded hot-plate measurements is relatively high at $1.0 \text{ mW m}^{-1} \text{K}^{-1}$ due to e.g. systematic deviations with the device and/or calibration, the reproducibility of the measurements is better than $0.5 \text{ mW m}^{-1} \text{K}^{-1}$, particularly for measurements on monolithic SCD plates.

2.4. Mechanical tests

Mechanical characterization of the SCD aerogels was performed on monolithic cylindrical samples using a universal mechanical testing setup (Zwick/Z010, Zwick/Roell, Germany), with a 2 kN force transducer (KAP-S, AST Gruppe GmbH, Germany) at 23°C and 50% RH. Samples were compressed at a rate of 1 mm/min up to 80% strain and elastic moduli were calculated from the linear regime of the curves (at $7 \pm 3\%$ strain). For the APD materials, no cylinders for uniaxial compression are available and therefore an alternative approach was considered. The mechanical test of the APD silica aerogel granulate were carried out using a micromechanical compression testing machine (FemtoTools) where the displacements are controlled with a stepper motor and compression forces measured with a capacitive load cell. The samples were compressed up to 50 μm at a rate of 1 $\mu\text{m/s}$ followed by decompression at the same rate. The compression tip has a square section with 50 μm side, i.e. much smaller than the ~2 mm large granules that were partially embedded in epoxy for fixation. The measurements were repeated 4-6 times, testing at different locations on the surface of the granules and the average stiffness value was calculated from the force-displacement curves. Note that with the micromechanical testing, only extrinsic properties can be calculated, e.g. stiffness, but not the elastic moduli. Because the area of the sample that experiences compression is larger than that of the tip, the area of material that resists against the compression is not well defined and the E modulus cannot be extracted from the force-displacement curves.

2.5. 3D simulations of λ through inter-particle necks

A full 3D picture of the silica aerogel microstructure, and the inter-particle necks in particular, remains beyond the spatial resolution of current imaging techniques. We therefore decided to simulate λ based on a simple geometric model that ignores the complex pore structure in silica aerogels. Similarly to previous work [52, 53], we base our calculations on the local λ of a contact of two overlapping spheres (5 nm diameter) within a surrounding gaseous media. However contrary to previous work, the contact region, representing both the pore and the solid pearl necklace structure was discretized into a network of local λ values [54], with a voxel size of 0.05 nm. The λ of the contact unit cell was calculated using a finite difference scheme and assuming constant temperature at the surfaces perpendicular to the direction of the temperature gradient and zero heat flux through the unit cell surfaces parallel to the heat flow. In this way any coupling effect between the solid and gas λ is taken into account implicitly. The model enables a qualitative comparison of λ across the different contacts, but most likely overestimates the absolute λ . The λ of the solid phase was assumed to be that of bulk amorphous silica ($1.35 \text{ W m}^{-1} \text{K}^{-1}$ [53]), i.e. we neglect the reduction of the solid λ due to the small size of the primary particles (5 nm) with respect to the phonon mean free path in amorphous silica (4 nm [55]). The gas phase λ most likely is overestimated because the local mean free path in the direction of the contact is infinite based on our unit cell. A full discussion on these limitations and the model is provided in the supporting information.

2.6. Synthesis of glued composites

For preparation of the composites ($50 \times 50 \times 10 \text{ mm}^3$), part of the granules were broken up into a fine powder with a blender. Granules (63 vol%) and powder (37 vol%) were then combined and stirred manually. Filling factors of the composites, defined as the bulk volume of the aerogel divided by the volume of the mould, were between 114% and 125%. Separately, a water-soluble glue was mixed with water and a small quantity of surfactant (0.08, 0.06 and 0.002 g for each cm^3 of sample volume, respectively). This solution was added to the aerogel mixture, stirred manually for five minutes, filled into a Teflon mould, compressed by tightening the screws on the mould, and left to cure under compression for 24 h under ambient conditions. The amount of surfactant was selected to enable sufficient wetting of the aerogels with the glue solution, but avoid excessive infiltration/degradation of the aerogel itself. After curing, the glue is located on the outside of the aerogel particles. Note that composites prepared from dense granulate and dense powders displayed significantly higher thermal conductivities, compared to “mixed” samples that comprised of both dense granulate and light powder, most likely because of the different compression behaviour during gluing.

3. Results and discussion

3.1. Silica aerogels produced by supercritical CO_2 drying

To clarify the effects of reduced skeletal conduction and densification as a result of APD, a series of identically aged reference gels of variable density were dried by SCD. Note that in contrast to APD, the SCD process limits shrinkage even for short-aged samples and the SCD aerogel density is determined primarily by the silica concentration in the sol, not by the aging time. The BET surface areas display only moderate variations as a function of density and aging time (Table S3). Consequently, the SCD aerogels display a systematic decrease in average pore diameter (calculated from the density and surface area) with increasing density: from ~60 to ~15

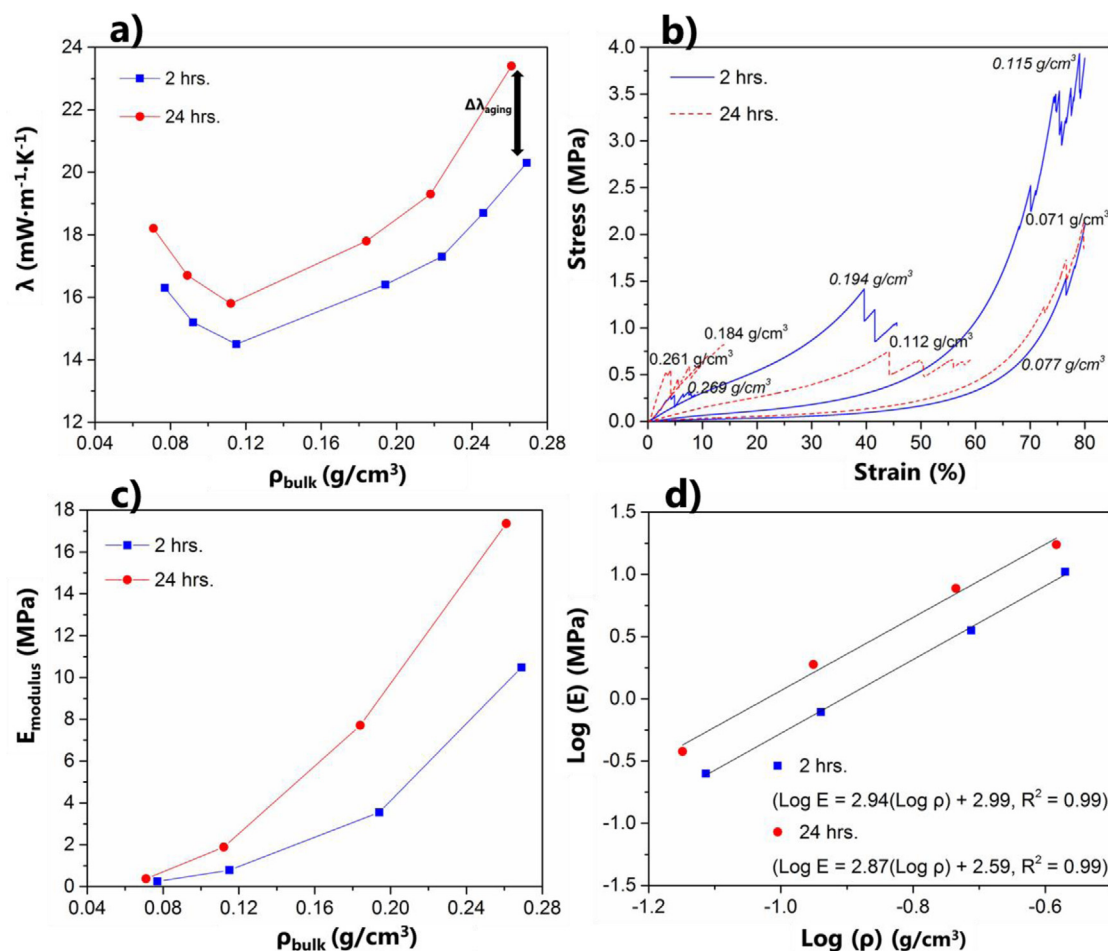


Figure 1. Properties of SCD silica aerogel reference samples as a function of aging time and density. The variation in density is due to variable silica precursor concentrations. a) λ versus ρ ; b) Compressive stress-strain curves; c) E versus ρ (linear plot); d) $\text{Log}(E)$ versus $\text{log}(\rho)$; the slopes are similar for both aging times, with α equal to 2.94 for 2 h aging and 2.87 for 24 h aging. The reproducibility on λ , ρ and E are estimated at $0.5 \text{ mW m}^{-1} \text{ K}^{-1}$, 2% and 5%, respectively.

nm for an increase in density from ~ 0.075 to $\sim 0.265 \text{ g/cm}^3$ (Table S3, Figures S1,S2).

The SCD reference aerogels display a typical dependence of thermal conductivity on density, with a minimum in λ at intermediate densities (Fig. 1a), with higher λ at lower density due to larger pore sizes (Figure S2) and higher λ at higher density due to an increase in solid conduction. Both the values of λ and their variation as a function of density are consistent with previous reports in the literature [21,23,24]. The sample with a density near $\sim 0.12 \text{ g/cm}^3$ has the lowest λ in this study, but the true minimum may be at somewhat higher densities, e.g. $\sim 0.14 \text{ g/cm}^3$ but no aerogels around this density have been prepared. A systematic offset to lower thermal conductivity is observed for samples prepared at the shortest aging time ($\Delta\lambda_{\text{aging}}$). $\Delta\lambda_{\text{aging}}$ amounts to $1.9 \text{ mW m}^{-1} \text{ K}^{-1}$ for the lowest ρ , decreases to $1.3 \text{ mW m}^{-1} \text{ K}^{-1}$ at the optimum in density, and increases to $3.0 \text{ mW m}^{-1} \text{ K}^{-1}$ for the highest density (Table S1). Aging increases λ_g , albeit to a small extent, because it leads to systematically lower surface areas and larger pore sizes (Table S3) and hence a less pronounced Knudsen effect. This mechanism will have the biggest impact on overall thermal conductivity at low density, where the contributions of λ_g are more prominent. Aging also increases λ_s , because it increases the cross-section of, and thermal transport through, the inter-particle necks that link up the primary silica particles, through a dissolution re-precipitation process akin to Ostwald ripening [41, 56, 57]. In addition, the connection of dangling particle chains to the rest of the particle network may increase the solid connectivity. The aging ef-

fect is most effective at high density, where the solid phase conduction is more dominant.

For both aging times, the stress (σ) – strain (ε) response of aerogels under uniaxial compression indicates that aerogels with $\rho > 0.2 \text{ g/cm}^3$ are brittle ($\varepsilon_{\text{max}} < 10\%$), while those with $\rho < 0.1 \text{ g/cm}^3$ can sustain at least 80% strain without breaking (Fig. 1b), consistent with an earlier report [24]. As expected, E displays a power-law ρ dependence ($E \sim \rho^{2.9}$) with a 40- to 50-fold increase in E for a 3- to 4-fold increase in ρ (Fig. 1c,d). A direct comparison to materials in other studies can be difficult because of variations in synthesis and measurement protocol. However, the value of 2.9 for the scaling exponent α is in line with previous experimental and modelling results for silica aerogels [24,26–29] and also the values of E are in line with those observed in previous studies on silica aerogel [24]. For a given ρ , increasing the aging time from 2 to 24 h, nearly doubles E (Fig. 1c, Table S1), because of the increased stiffness in the gel network due to the strengthening of the solid network structure and the inter-particle necks in particular [56,57], but this effect is small compared to the much larger effect of density.

3.2. Silica aerogels produced by ambient pressure drying

3.2.1. Density and thermal conductivity

Considering the APD materials, we observed that in addition to the expected density induced strengthening, the structural collapse leads to a surprisingly low thermal conductivity for a given density.

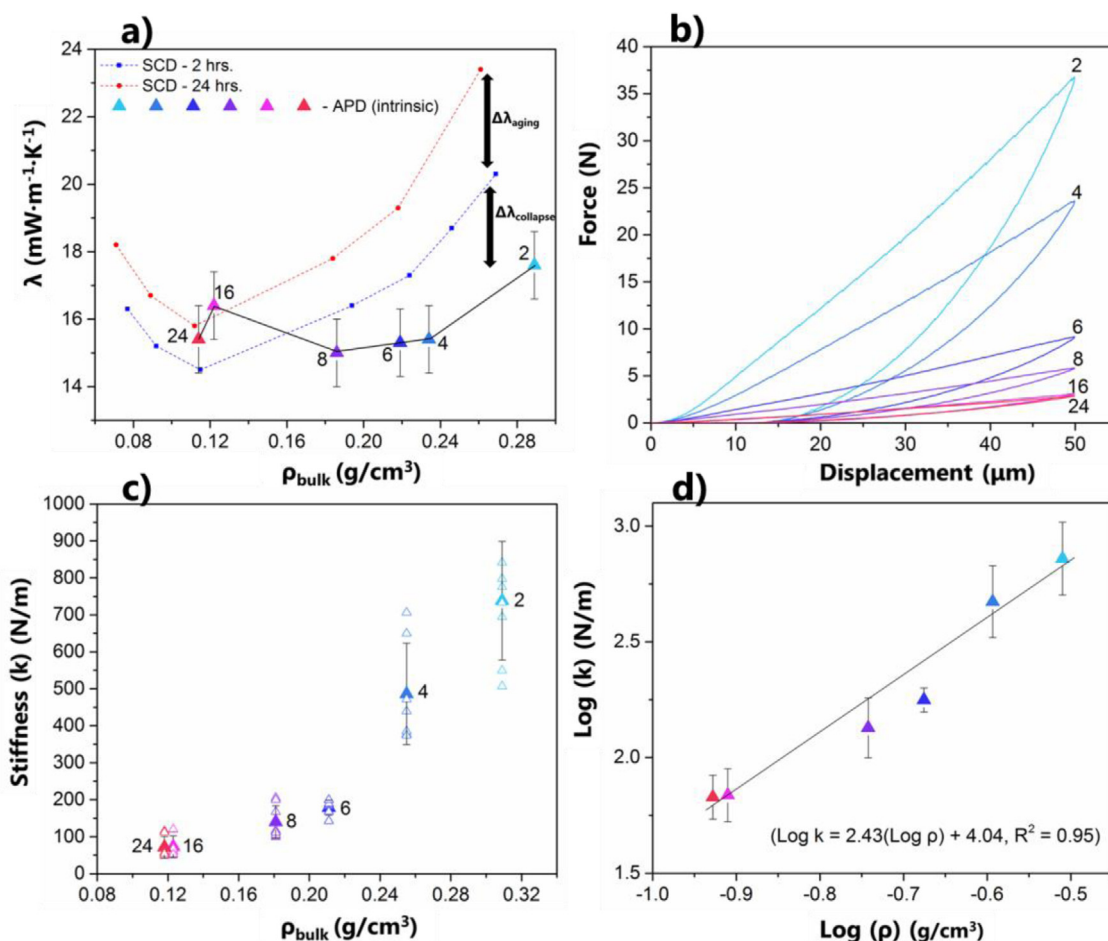


Figure 2. Properties of APD silica aerogel as a function of aging time and density. The variation in density results from aging time dependent pore collapse. a) λ versus ρ for a SiO_2 equivalent concentration of $0.057 \text{ g}/\text{cm}^3$; the intrinsic λ was determined with the procedure of Huber et al. [49] (Table S2); b) Force displacement curves; c) Stiffness (k) versus ρ (linear plot) where the open symbols are individual measurements and the filled symbols denote the average; d) $\text{Log}(k)$ versus $\text{log}(\rho)$. Numbers next to the data markers denote the aging time in hours. The uncertainty on λ and ρ are estimated at $1.0 \text{ mW m}^{-1} \text{ K}^{-1}$ and 4%, respectively.

Note that the variation in density for the APD samples is due to the aging time dependent pore collapse, rather than precursor concentration as for the SCD aerogels. The nitrogen sorption isotherms as a function of aging time have been reported for APD aerogels produced with the same protocol in a previous study [41]. With increasing aging time from 2 to 24 h, the surface area decreases from 901 to 816 m^2/g and the average pore diameter increases from 12 to 39 nm.

The thermal conductivity of the APD silica aerogel with a density near $0.12\text{--}0.14 \text{ g}/\text{cm}^3$ is in line with other APD silica aerogels from the literature [49,58–60] and commercial silica aerogel granulate. The variation of the intrinsic λ of APD silica aerogel granulate is plotted as a function of density in Fig. 2a. Most strikingly, the intrinsic λ remains near $15 \text{ mW m}^{-1} \text{ K}^{-1}$ even for $\rho \sim 0.24 \text{ g}/\text{cm}^3$, which challenges the understanding that silica aerogel only display $\lambda \sim 15 \text{ mW m}^{-1} \text{ K}^{-1}$ for density values around $0.12 \text{ g}/\text{cm}^3$ [22,24]. The very low thermal conductivity of the short aged, high density silica granulate cannot be fully explained by aging-induced Ostwald ripening and dangling chain effects alone (Figure 3b), as $\Delta\lambda_{\text{aging}}$ is limited to $2\text{--}3 \text{ mW m}^{-1} \text{ K}^{-1}$ based on the SCD data (Figs. 1 and 2a). The additional offset in thermal conductivity, designated here as $\Delta\lambda_{\text{collapse}}$ has a magnitude of up to $4 \text{ mW m}^{-1} \text{ K}^{-1}$, and must thus be related to the APD induced partial pore collapse (Figure 3c) [21]. Combined, $\Delta\lambda_{\text{aging}}$ and $\Delta\lambda_{\text{collapse}}$ amount to a difference in λ of $6 \text{ mW m}^{-1} \text{ K}^{-1}$ for aerogels with the same density but different synthesis protocol (SCD, long aging versus

APD short aging, Fig. 2a). The additional offset in thermal conductivity of the partially collapsed APD aerogels most likely is related to two main factors: i) low solid conduction through the point contacts formed during APD induced partial pore collapse (see Section 3.2.2) and ii) a possible further reduction of the gas phase conduction because of a preferential decrease in pore size of the larger pores, under the assumption that larger pores represent weaker areas of the gel that are more prone to collapse than smaller pores. In the absence of thermal conductivity data collected at low pressure [50], the relative importance of both effects cannot be determined quantitatively. However, the fact that this effect is so prominent at high aerogel densities, where solid conduction is the dominant heat transport mechanism, indicates the importance of the former process (i).

3.2.2. Heat transport through inter-particle necks

Solid heat conduction in aerogels is affected by both the tortuosity of the solid network and the contacts between the primary as well as secondary (porous) particles that make up the aerogel backbone. During densification, secondary particles may merge and their empty pore space may accommodate primary particles from neighbouring assemblies [61]. At the same time, the secondary particles themselves may densify. Both processes create new contacts between primary particles. The inter-particle necks play a key role for solid heat conduction [52,53,62,63]. Because (3D)-imaging the necks at the required resolution is not feasible due to their

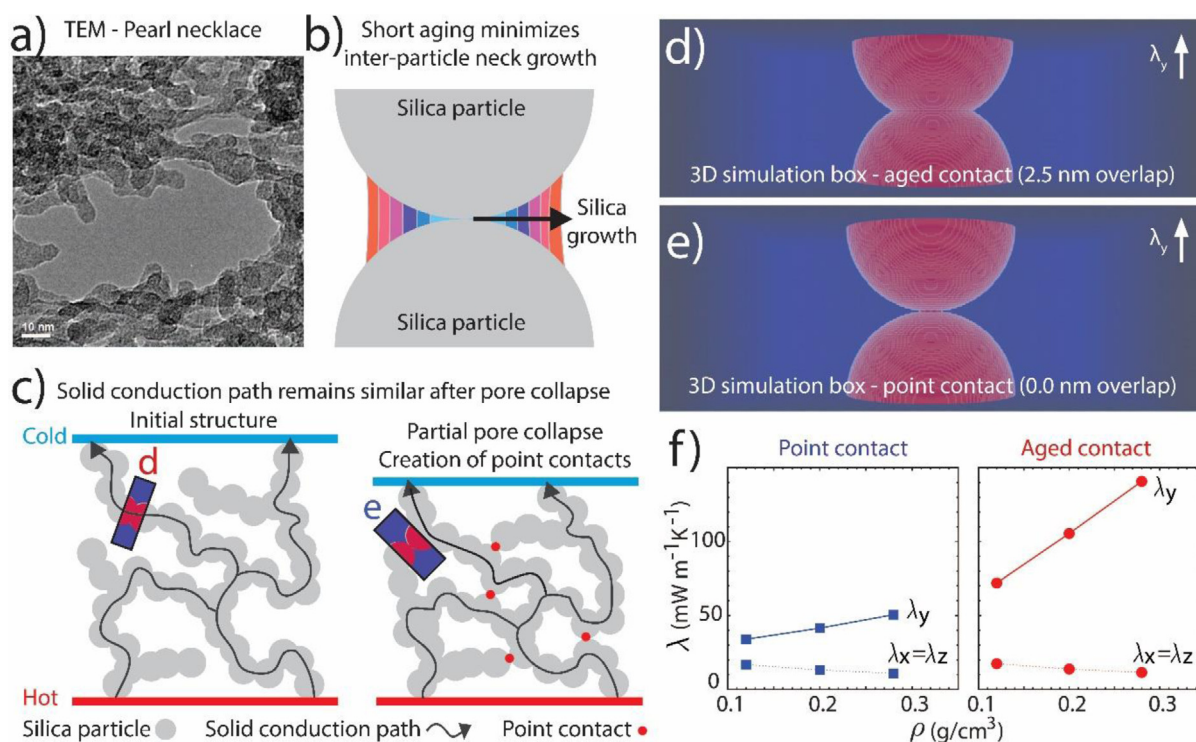


Figure 3. Strongly reduced λ_s in high ρ , low λ silica aerogels. a) TEM image of silica aerogel. b) Growth of silica in the inter-particle necks. c) Schematic illustration of solid heat conduction paths for an initial and collapsed structure as well as local structures that resemble the unit cells used for the calculations (sub-figure d and e). d) Calculation box for an aged contact between 2 silica particles. e) Calculation box for a point contact between 2 silica nanoparticles. f) Modelled λ parallel (λ_y) and orthogonal (λ_x, λ_z) to the particle chain as a function of ρ_{bulk} .

instability in the electron beam, we modelled the heat transport through a neck composed of two overlapping spheres (Supporting Information). The simulated λ values are much higher across an inter-particle neck with a significant cross section compared to a point contact, particularly in the direction parallel to the particle chain, λ_y (Fig. 3d-f). For the model aged contact, the strong increase in λ_y with increasing density can no longer be compensated by the decrease in λ_x and λ_z related to the (small) reduction in pore size and gas phase conduction (Fig. 3f). Long and short aged SCD silica aerogel have a single type of inter-particle neck with large and small cross sections, respectively, and this difference accounts for the observed $\Delta\lambda_{\text{aging}}$ (Fig. 2a). The short-aged APD silica aerogel has at least two types of inter-particle necks: i) contacts generated during the sol-gel step with a small cross section because the short aging limited silica growth at the inter-particle neck, and ii) new contacts generated during the partial pore collapse that are closer to true point contacts because prior surface silylation effectively prevented further Si-O-Si condensation and neck growth. The limited heat flow through these point contacts (Fig. 3f) means that only few new heat conduction paths are created during drying-induced partial pore collapse and densification (Fig. 3c). Similar point contacts may be present in silica aerogels densified irreversibly by uniaxial compression during a separate, post-production step. [51,64]

3.2.3. Mechanical properties of APD aerogels

The increase in density with decreasing aging time for the APD aerogels leads to a marked increase in the stiffness (Fig. 2b,c). Similar to the E modulus of SCD aerogels, the stiffness (k) displays a power law dependence on density ($k \sim \rho^{2.4}$), with a 10-fold increase in stiffness for a 2.4-fold in density (Fig. 2d, Table S2). Thus, the high density APD silica aerogels are stiffer by an order of magnitude over conventional silica aerogel, but retain the ultra-low λ . In contrast to the monolithic SCD silica aerogel, for which extensive

mechanical datasets are available in the literature, few mechanical data are available for silica aerogel granulate. As in this study, Very recently, Hamelin et al. carried out compression testing on individual granules, but in contrast to our micro-penetration study, they used compression plates with areas larger than the individual granules [65]. As a result, their study provided a unique look into the effect of granule morphology and density on fracture properties, but was less informative about the stiffness of the material itself.

3.2.4. Composites from dense, but superinsulating silica aerogels

Strong, superinsulating silica aerogel granulate is an attractive fillers for applications where the final product benefits from the unique combination of thermal and mechanical properties, for example aerogel composite boards, concrete, gypsum boards, renders or 3D printing [9]. A higher volume fraction of high ρ , low λ granulate could be added without compromising the composite mechanical properties, leading to a lower λ at the same mechanical performance. Alternatively, a substantially higher mechanical strength is attainable for the same composite λ . As a first, not yet fully optimized demonstration, we present the benefits of including high ρ , low λ aerogel granulate into glued aerogel composites (Fig. 4). The increased stiffness of dense aerogel granulate almost triples the E-modulus and nearly doubles the final compressive strength of the glued aerogel composites compared to one produced with standard density silica aerogel granulate, with only a limited penalty in thermal conductivity (5-14%) (Table 1). Note that based on our experience in compounding aerogels the glue is estimated to increase thermal conductivity by ca. 2-3 mW m⁻¹ K⁻¹ for both composites, produced from standard density or high density aerogel.

Table 1
Thermo-mechanical properties of glued composites.

Aging time (h) (G+P for mixed samples)	λ (mW m ⁻¹ K ⁻¹)	E (MPa)	σ_{max} (MPa)
For a nominal filling factor ^{a)} of 125% ^{b)}			
24	20.7	0.117	0.105
24	20.1	0.124	0.160
2+24	21.5	1.017	0.850
2+24	21.3	0.479	0.265
24+2	22.3	0.254	0.415
24+2	20.9	0.098	0.113
For a nominal filling factor ^{c)} 114% ^{b)}			
24	18.1	0.300	0.037
24	18.1	0.241	0.038
2+24	20.6	0.766	0.066
2+24	20.7	0.770	0.059

G - granulate, P - powder

^{a)} Filling factor of aerogel inside the mould during gluing, $V_{env}/V_{mold}=(m_G/\rho_G+m_P/\rho_P)/V_{mold}$.

^{b)} 50 × 50 × 10 mm³ plates for both the λ measurements and compression tests

^{c)} 50 × 50 × 10 mm³ plates for λ measurements, 30 × 30 × 30 mm³ cubes for compression tests

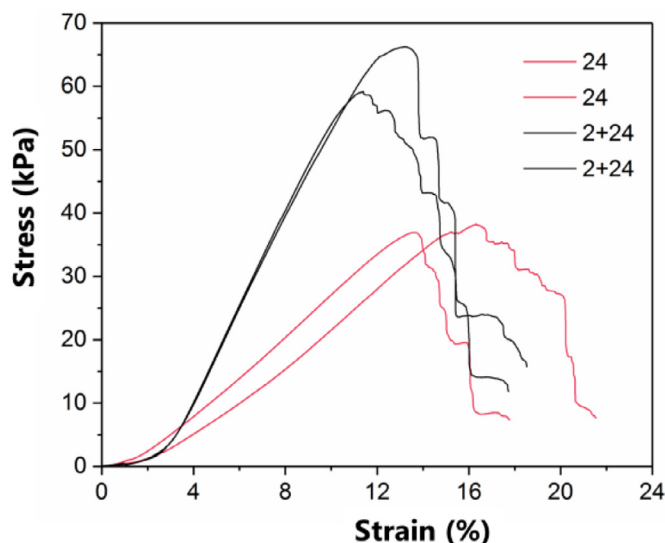
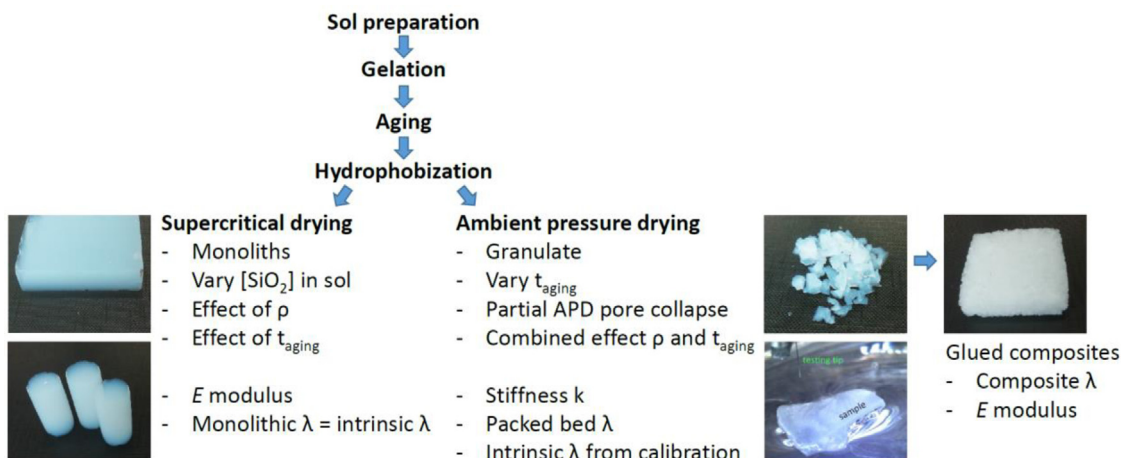


Figure 4. Compression curves of glued aerogel composites. The “24” curves correspond to glued composites prepared with conventional granulate and powder (24 h aging). The “2+24” curves contain high ρ , low λ granulate (2 h aging, 63 vol%) and conventional silica aerogel powder (24 h aging, 37 vol%).

4. Conclusions

The general view of silica aerogel is that of a superinsulating, but mechanically poor material. Aside from cost, these lacklustre mechanical properties limit a widespread adoption far beyond their niche application of pipeline insulation. Our discovery of ultra-low λ silica aerogel granulate that is an order of magnitude more stiff than conventional silica aerogel can change the perception of silica aerogels as weak and costly materials, and allow the advance of the next generation silica aerogel into new, structural applications. The lower thermal conductivity is the result of short aging to limit the growth of thick inter-particle necks and the concomitant increase in thermal conductivity. In addition, shorter aging results in (slightly) larger pore sizes and may reduce the probability to connect dangling particle chains to the rest of the network. Finally, new contacts formed during drying-induced partial pore collapse can be considered as true point contacts because the surfaces have been hydrophobized (passivated) prior to drying. The modelling and experimental data indicate that, while these newly formed point contacts do not increase thermal conductivity of the densified aerogels, they do increase the resistance against compression, i.e. stiffness. This effectively decouples thermal conductivity and mechanical strength, which are often correlated because of their co-dependency on network connectivity (tortuosity and inter-particle necks). Of practical importance, the increase in



Scheme 1. Aerogel synthesis and characterization strategy.

stiffness is simply due to a densification of the silica matrix and does not rely on the addition of polymer co-precursors or reinforcing agents that may deteriorate the fire behaviour and high-temperature stability. In addition, this new type of strong, superinsulating silica aerogels are synthesized with a shorter processing time (reduced by 10–50% due to shorter aging) and are accessible by ambient pressure drying, which eliminates the cost intensive SCD process commonly used for polymer or polymer-reinforced aerogel processing.

Supporting information

Table S1: Thermo-mechanical properties of SCD silica aerogels.

Table S2: Thermo-mechanical properties of APD silica aerogels.

Table S3: Different properties of SCD silica aerogels.

Table S4: Calculated thermal conductivities λ of particle contacts with different envelope densities (ρ_{bulk} , assuming a solid density of 2.0 g/cm³), and diameter of the contact are between primary particles (d_{contac}). Calculated conductivities are reported in the x, y and z direction, where the particle contact is arranged in the y direction. Also shown are averaged values assuming a serial (λ_{ser}) and parallel (λ_{par}) arrangement of contacts in different direction as well as a parallel arrangement of λ_{ser} and λ_{par} (λ_{av}). Also reported are other physical properties of the particle contact unit cell, such as the specific surface area (A_{spec}), the surface per volume ratio of the pores ($A_{\text{pore}}/V_{\text{pore}}$) and the average pore size calculated using the maximum included sphere method (d_{por}).

Figure S1. Nitrogen sorption isotherms of SCD silica aerogels for different starting silica concentrations aged at (a) 2hrs. and (b) 24 hrs.

Figure S2. (a) Influence of starting silica concentration on pore diameter and (b) thermal conductivity (λ) as a function of pore diameter of SCD silica aerogels aged at 2 hrs. and 24 hrs. respectively.

Figure S3. a) Discretized primary particle contact unit cell used for the numerical calculations. b) Assumed periodicity for calculation of mean free path in the gas phase. c) Schematic view of estimation of the macroscopic thermal conductivity based on the calculation of the thermal conductivity of the particle contact unit cell in different direction, where λ_{par} assumes parallel resistances with the pearl necklace structure arranged in different directions; λ_{ser} assumes serial resistances and finally λ_{avg} a parallel arrangement of λ_{par} and λ_{ser} . In our model, a change of structure and density influences both the local gas conductivities as well as the relative importance of the conduction through the solid backbone.

Figure S4. Evolution of the calculated conductivities with increasing particle contact radius (a) and with increasing envelope density (b). The points shown correspond to the averaged thermal conductivity λ_{avg} , while the error bars are the parallel and serial limits (λ_{par} and λ_{ser}).

Figure S5. Thermal conductivity as a function of the E modulus for SCD aerogels for 2 different aging times. The variation seen is the result of the density dependencies of the thermal conductivity and the E modulus.

Declaration of Competing Interest

Empa owns equity in patent application EP3498672A1 about the use of high ρ , low λ silica aerogel for insulation applications.

Acknowledgements

We thank Dr. Geert Snellings (Recticel N.V.) for his suggestions and input. We are also grateful to Shanyu Zhao for discussions, Beatrice Fischer for providing access to the Zwick press and

Yucheng Zhang for TEM analysis. We thank the Flemish agency 'Agentschap Innoveren en Ondernemen' for financial support.

Supplementary materials

Supplementary material associated with this article can be found, in the online version, at doi:[10.1016/j.actamat.2021.116959](https://doi.org/10.1016/j.actamat.2021.116959).

References

- [1] S.S. Kistler, Coherent expanded aerogels and jellies, *Nature* 127 (1931) 741–741.
- [2] M.A. Aegerter, N. Leventis, M.M. Koebel, *Aerogels Handbook*, Springer-Verlag, New York, 2011.
- [3] I. Smirnova, S. Suttiruengwong, W. Arlt, Feasibility study of hydrophilic and hydrophobic silica aerogels as drug delivery systems, *J. Non Cryst. Solids* 350 (2004) 54–60.
- [4] C. Zhu, et al., Highly compressible 3D periodic graphene aerogel microlattices, *Nat. Commun.* 6 (2015) 6962.
- [5] R.T. Olsson, et al., Making flexible magnetic aerogels and stiff magnetic nanopaper using cellulose nanofibrils as templates, *Nat. Nanotechnol.* 5 (8) (2010) 584.
- [6] A.E. Aliev, et al., Giant-stroke, superelastic carbon nanotube aerogel muscles, *Science* 323 (5921) (2009) 1575–1578.
- [7] D.R. Rolison, Catalytic nanoarchitectures—the importance of nothing and the unimportance of periodicity, *Science* 299 (5613) (2003) 1698–1701.
- [8] N. Ganonyan, et al., Entrapment of enzymes in silica aerogels, *Mater. Today* (2019).
- [9] S. Zhao, et al., Additive manufacturing of silica aerogels, *Nature* 584 (7821) (2020) 387–392.
- [10] R. Baetens, B.P. Jelle, A. Gustavsen, Aerogel insulation for building applications: a state-of-the-art review, *Energy Build.* 43 (2011) 761–769.
- [11] T. Woignier, J. Phalippou, Mechanical strength of silica aerogels, *J. Non Cryst. Solids* 100 (1–3) (1988) 404–408.
- [12] M.A.B. Meador, L.A. Capadona, *Process for Preparing Polymer Reinforced Silica Aerogels*, 2011.
- [13] M.A.B. Meador, et al., Cross-linking amine-modified silica aerogels with epoxies: mechanically strong lightweight porous materials, *Chem. Mat.* 17 (2005) 1085–1098.
- [14] N. Leventis, et al., Nanoengineering strong silica aerogels, *Nano Lett.* 2 (9) (2002) 957–960.
- [15] B.N. Nguyen, et al., Tailoring elastic properties of silica aerogels cross-linked with polystyrene, *ACS Appl. Mater. Interfaces* 1 (3) (2009) 621–630.
- [16] S. Zhao, et al., Strong, thermally superinsulating biopolymer-silica aerogel hybrids by cogelation of silicic acid with pectin, *Angew. Chem. Int. Ed.* 127 (2015) 14490–1494.
- [17] G. Zhang, et al., Isocyanate-crosslinked silica aerogel monoliths: preparation and characterization, *J. Non Cryst. Solids* 350 (2004) 152–164.
- [18] H. Maleki, L. Durães, A. Portugal, Synthesis of mechanically reinforced silica aerogels via surface-initiated reversible addition-fragmentation chain transfer (RAFT) polymerization, *J. Mater. Chem. A* 3 (4) (2015) 1594–1600.
- [19] K. Kanamori, et al., New transparent methylsilsesquioxane aerogels and xerogels with improved mechanical properties, *Adv. Mater.* 19 (12) (2007) 1589–1593.
- [20] X. Lu, et al., Thermal conductivity of monolithic organic aerogels, *Science* 255 (5047) (1992) 971–972.
- [21] J. Fricke, et al., Optimization of monolithic silica aerogel insulants, *Int. J. Heat Transfer* 35 (1992) 2305–2309.
- [22] N. Hüsing, U. Schubert, Aerogels—airy materials: chemistry, structure, and properties, *Angew. Chem. Int. Ed.* 37 (1998) 22–45.
- [23] X. Lu, et al., Thermal transport in organic and opacified silica monolithic aerogels, *J. Non Cryst. Solids* 145 (1992) 207–210.
- [24] J.C.H. Wong, et al., Mechanical properties of monolithic silica aerogels made from polyethoxydisiloxanes, *Micropor. Mesopor. Mat.* 183 (2014) 23–29.
- [25] S. Zhao, et al., Biopolymer Aerogels and Foams: Chemistry, Properties and Applications, *Angew. Chem. Int. Ed.* 57 (2018) 7580–7608.
- [26] T. Woignier, et al., Different kinds of structure in aerogels: relationships with the mechanical properties, *J. Non Cryst. Solids* 241 (1) (1998) 45–52.
- [27] S.P. Patil, et al., Mechanics of nanostructured porous silica aerogel resulting from molecular dynamics simulations, *J. Phys. Chem. B* 121 (22) (2017) 5660–5668.
- [28] J.S.R. Murillo, et al., Structure and mechanical properties of silica aerogels and xerogels modeled by molecular dynamics simulation, *J. Non Cryst. Solids* 356 (25–27) (2010) 1325–1331.
- [29] J. Lei, et al., Determination of the Young's modulus of silica aerogels—an analytical-numerical approach, *Soft Matter* 9 (47) (2013) 11367–11373.
- [30] C.A. Ferreira-Rangel, L.D. Gelb, Investigation of the bulk modulus of silica aerogel using molecular dynamics simulations of a coarse-grained model, *J. Phys. Chem. B* 117 (23) (2013) 7095–7105.
- [31] H. Ma, et al., *Simulation and analysis of mechanical properties of silica aerogels: from rationalization to prediction*, *Materials* 11 (2) (2018) 214.
- [32] S.P. Patil, P. Shendye, B. Markert, *Mechanical properties and behavior of glass fiber-reinforced silica aerogel nanocomposites: insights from all-atom simulations*, *Scr. Mater.* 177 (2020) 65–68.

- [33] S.P. Patil, P. Shendye, B. Markert, *Molecular dynamics simulations of silica aerogel nanocomposites reinforced by glass fibers, graphene sheets and carbon nanotubes: a comparison study on mechanical properties*, *Compos. Part B: Engineering* 190 (2020) 107884.
- [34] S.P. Patil, et al., *Fracture of silica aerogels: an all-atom simulation study*, *J. Non Cryst. Solids* 498 (2018) 125–129.
- [35] H.-P. Ebert, in: *Thermal Properties of Aerogels*, in *Aerogels Handbook*, Springer, 2011, pp. 537–564.
- [36] X. Lu, et al., *Correlation between structure and thermal conductivity of organic aerogels*, *J. Non Cryst. Solids* 188 (3) (1995) 226–234.
- [37] J.K. Lee, G.L. Gould, W. Rhine, *Polyurea based aerogel for high performance thermal insulation*, *J. Sol-Gel Sci. Technol.* 49 (2009) 209–220.
- [38] Z. Zhu, et al., *Superinsulating polyisocyanate based aerogels: a targeted search for the optimum solvent system*, *ACS Appl. Mater. Interfaces* 9 (21) (2017) 18222–18230.
- [39] G. Hayase, et al., *The thermal conductivity of polymethylsilsesquioxane aerogels and xerogels with varied pore sizes for practical application as thermal superinsulators*, *J. Mater. Chem. A* 2 (18) (2014) 6525–6531.
- [40] G. Zu, et al., *Transparent, superflexible doubly cross-linked polyvinylpolymethylsiloxane aerogel superinsulators via ambient pressure drying*, *ACS Nano* 12 (1) (2018) 521–532.
- [41] S. Iswar, et al., *Effect of aging on silica aerogel properties*, *Micropor. Mesopor. Mat.* 241 (2017) 292–302.
- [42] G.M. Pajonk, et al., *Physical properties of silica gels and aerogels prepared with new polymeric precursors*, *J. Non Cryst. Solids* 186 (1995) 1–8.
- [43] S.S. Prakash, et al., *Silica aerogel films prepared at ambient pressure by using surface derivatization to induce reversible drying shrinkage*, *Nature* 374 (1995) 439–443.
- [44] S. Brunauer, P.H. Emmett, E. Teller, *Adsorption of gases in multimolecular layers*, *J. Am. Chem. Soc.* 60 (1938) 309–319.
- [45] A. Ayril, J. Phalippou, T. Woignier, *Skeletal density of silica aerogels determined by helium pycnometry*, *J. Mater. Sci.* 27 (5) (1992) 1166–1170.
- [46] E.P. Barrett, L.G. Joyner, P.P. Halenda, *The determination of pore volume and area distributions in porous substances. I. Computations from nitrogen isotherms*, *J. Am. Chem. Soc.* 73 (1951) 373–380.
- [47] G. Reichenauer, *Structural characterization of aerogels*, in: *Aerogels Handbook*, Springer, New York, 2011, pp. 449–498. M.A. Aegerter, N. Leventis, and M.M. Koebel, Editors.
- [48] T. Stahl, et al., *Thermo-hygric properties of a newly developed aerogel based insulation rendering for both exterior and interior applications*, *Energy Build.* 44 (2012) 114–117.
- [49] L. Huber, et al., *Fast and minimal-solvent production of superinsulating silica aerogel granulate*, *Angew. Chem. Int. Ed.* 56 (2017) 4753–4756.
- [50] M. Reim, et al., *Silica-aerogel granulate—structural, optical and thermal properties*, *J. Non Cryst. Solids* 350 (2004) 358–363.
- [51] A. Neugebauer, et al., *Thermal conductivity and characterization of compacted, granular silica aerogel*, *Energy Build.* 79 (2014) 47–57.
- [52] K. Swimm, et al., *Gas pressure dependence of the heat transport in porous solids with pores smaller than 10 μm* , *Int. J. Thermophys.* 30 (4) (2009) 1329–1342.
- [53] S. Zeng, A. Hunt, R. Greif, *Geometric structure and thermal conductivity of porous medium silica aerogel*, *J. Heat Transfer* 117 (4) (1995).
- [54] B. Derrida, et al., *A transfer matrix program to calculate the conductivity of random resistor networks*, *J. Stat. Phys.* 36 (1–2) (1984) 31–42.
- [55] L. Yang, et al., *Ballistic phonon penetration depth in amorphous silicon dioxide*, *Nano Lett.* 17 (12) (2017) 7218–7225.
- [56] P.J. Davis, C.J. Brinker, D.M. Smith, *Pore structure evolution in silica gel during aging/drying I. Temporal and thermal aging*, *J. Non Cryst. Solids* 142 (1992) 189–196.
- [57] G.W. Scherer, *Aging and drying of gels*, *J. Non Cryst. Solids* 100 (1–3) (1988) 77–92.
- [58] R.G. Martinez, et al., *Thermal assessment of ambient pressure dried silica aerogel composite boards at laboratory and field scale*, *Energy Build.* 128 (2016) 111–118.
- [59] Y. Jiang, J. Feng, J. Feng, *Synthesis and characterization of ambient-dried microglass fibers/silica aerogel nanocomposites with low thermal conductivity*, *J. Sol-Gel Sci. Technol.* 83 (1) (2017) 64–71.
- [60] Y. Huang, et al., *Organic solvent-saving preparation of water glass based aerogel granules under ambient pressure drying*, *J. Non Cryst. Solids* 521 (2019) 119507.
- [61] C. Mandal, et al., *Experimental deconvolution of depressurization from capillary shrinkage during drying of silica wet-gels with SCF CO₂ why aerogels shrink? J. Sol-Gel Sci. Technol.* 92 (3) (2019) 662–680.
- [62] G. Wei, et al., *Thermal conductivities study on silica aerogel and its composite insulation materials*, *Int. J. Heat Mass Transfer* 54 (11–12) (2011) 2355–2366.
- [63] T. Xie, Y.-L. He, Z.-J. Hu, *Theoretical study on thermal conductivities of silica aerogel composite insulating material*, *Int. J. Heat Mass Transfer* 58 (1–2) (2013) 540–552.
- [64] G.L. Gould, et al., *High Strength, Nanoporous Bodies Reinforced with Fibrous Materials*, 2009.
- [65] G. Hamelin, et al., *Mechanical properties of milimetric silica aerogel particles produced through evaporative drying: a coupled experimental and discrete element approach*, *J. Non Cryst. Solids* 560 (2021) 120727.